New high permittivity tetragonal tungsten bronze dielectrics $Ba_2LaMNb_4O_{15}$: M=Mn, Fe

Emma E. McCabe, Anthony R. West *

Department of Engineering Materials, University of Sheffield, Mappin Street, Sheffield, S1 3JD, UK

ARTICLE INFO

ABSTRACT

The new phases $Ba_2LaMNb_4O_{15}$: M=Mn, Fe were prepared by solid state reaction at 1100 °C. They have the tetragonal tungsten bronze structure, space group $P4/mbm$, at room temperature. The two octahedral sites show partial order of M and Nb with preferential occupancy of the smaller $B(1)$ sites by M. Both phases have high permittivities 90 ± 15 over the range 10–320 K. $Ba_2LaFeNb_4O_{15}$ is highly insulating with bulk conductivity $\ll 10^{-8}$ ohm^{-1} cm^{-1} at 25 °C and $\tan \delta \ll 0.001$ over the range 100–320 K and at 10^5 Hz. Solid solutions between these new phases and the compositionally and structurally related relaxor ferroelectric $Ba_2LaTi_2Nb_3O_{15}$ show gradual loss of ferroelectric behaviour attributed to replacement of polarisable Ti^{4+} by a mixture of $(Mn, Fe)^{3+}$ and Nb^{5+}.

© 2010 Published by Elsevier Inc.

1. Introduction

The tetragonal tungsten bronze (TTB) family of complex oxides contains a number of phases that are ferroelectric [1–3]. One fairly well-characterised group of materials has the general formula $Ba_2RETi_2Nb_3O_{15}$ (RE=La, Pr, Nd, Sm, Eu, Gd, Dy and Bi) [4–9]. These show an interesting variation in properties with size of the rare earth cation: the ferroelectric Curie temperature, T_C, increases with decreasing rare earth ion size from ~200 K for RE=La [8,9] to ~600 K for RE=Gd [5]. At the same time, the electrical properties change from relaxor ferroelectric (RE=La) to first order behaviour with a sharp permittivity maximum at T_C for RE=Nd and smaller RE cations [6]. It was suggested that T_C depends on the size difference between Ba and RE cations that are ordered on the A and A' sites, respectively.

The TTB structure has much scope for variation in its chemical composition. The general formula may be written as $A_2A'CB_2B_3'O_{15}$, in which the A sites contain large ions such as alkalis, alkaline earths and rare earths; B sites contain octahedral cations such as Ti^{4+} and Nb^{5+}; the C sites are usually empty. The structure shown in Fig. 1 has a framework of corner-linked BO_6 octahedra which enclose channels for the A cations running parallel to the c axis.

Detailed structural studies of $Ba_2LaTi_2Nb_3O_{15}$ below and above T_C show that both octahedral B sites exhibit off-centre displacement of cations below T_C and both contain a non-random mixture of Nb and Ti. However, the existence of two crystallographically

distinct non-centrosymmetric sites, each with a mixture of two polarisable cations further complicates understanding of the ferroelectric properties. In other ferroelectric structures such as $BaTiO_3$ and $KNbO_3$, both Ti and Nb are able to occupy non-centrosymmetric, distorted octahedral sites that are responsible for the low temperature ferroelectric properties [10]. Hence either Ti or Nb, or both cations, could be responsible for the ferroelectric properties of the TTB phases.

TTB phases often exhibit complex superstructures which may be commensurate or incommensurate. In $Ba_2(La,Nd)Ti_2Nb_3O_{15}$, a complex sequence of structural changes with temperature was observed by selected area electron diffraction, involving phase changes between different superstructures, as well as the symmetry change at T_C [7]. An unusual hysteresis of 50–100 °C between T_C values on heating and cooling was observed for RE=Nd, Sm analogues, together with a huge depression of the Curie–Weiss temperature T_O, obtained by extrapolation of the high permittivity, ε', data to a value of $(\varepsilon')^{-1}$=0 at low temperatures [11]. Both these effects were attributed to deconvolution of the structural changes around T_C into two components, one associated with a change in the superstructure from commensurate to incommensurate, and the other to a change from a centrosymmetric space group to a non-centrosymmetric one that is responsible for the paraelectric to ferroelectric transition on cooling [11]. Further complexity in the electrical properties arises in solid solutions between TTB phases; for instance, in the series $Sr_2(La_xNd_{1-x})Ti_2Nb_3O_{15}$, intermediate compositions show a complex ε' vs T profile with up to four maxima [12].

The purpose of this study was to investigate consequences of introducing paramagnetic cations onto the B site; if ferroelectric

---

* Corresponding author.
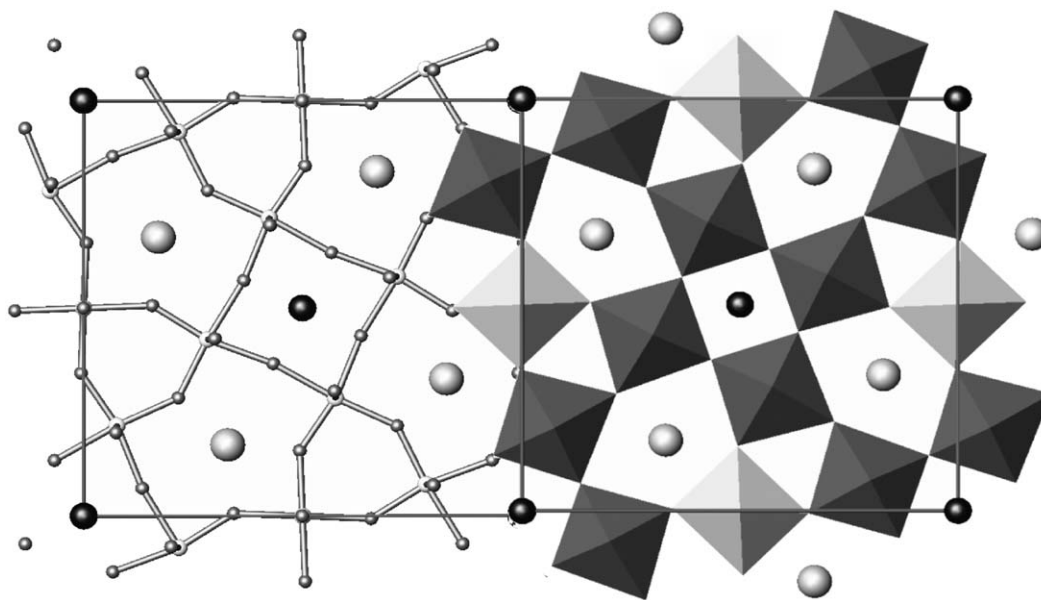E-mail address: A.R.West@sheffield.ac.uk (A.R. West).

Fig. 1. An *ab* projection of the TTB crystal structure; two unit cells are shown highlighting the *B*–O bonds (left) and *B*O$_6$ octahedra (right) with divalent and trivalent *A* cations shown as large grey and black spheres, respectively, and *A* cations shown in white spheres with oxygen anions shown as small grey spheres. *B*(1)O$_6$ and *B*(2)O$_6$ polyhedra are shaded in light and dark grey, respectively.

properties could persist at significant substitution levels, then the potential for combining both magnetic and ferroelectric properties in a TTB material might be realised. Since most studies so far had focused on Ti and Nb analogues, together with the existence of similar Ta-containing phases, we considered the effect of replacing Ti in a double substitution mechanism:

$$2Ti^{4+} \rightarrow Mn^{3+}/Fe^{3+} + Nb^{5+}.$$
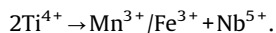
Assuming Mn and Fe possess trivalent oxidation states, no other compositional change should be required to achieve electrical neutrality. Complete replacement of Ti was found in both cases, yielding the new phases Ba$_2$LaMNb$_4$O$_{15}$: M=Mn, Fe. Given the possible existence of other rare earth analogues as well as phases containing Sr instead of Ba and Ta instead of Nb, a very large number of phases with this general formula may be anticipated. Whilst this manuscript was in preparation, Castel et al. reported investigations into composites of Ba$_2$LaFeNb$_4$O$_{15}$ and Fe$_2$O$_3$ with evidence for some dielectric relaxation and ferromagnetism for 5% Fe$_2$O$_3$ contents [13]. However, consistent with our results reported in this work, no dielectric anomaly was observed for pure Ba$_2$LaFeNb$_4$O$_{15}$.

The two new phases, Ba$_2$LaMNb$_4$O$_{15}$: M=Mn, Fe, are not ferroelectric but nevertheless retain high polarisability in their crystal structures. This, coupled with their highly insulating behaviour, indicates possible applications as dielectric materials, either in thin film form or as microwave dielectrics—assuming that their electrical properties measured at 10^5 Hz persist to microwave frequencies [14].

2. Experimental

Two sets of materials were prepared with general formula Ba$_2$LaTi$_{2-2x}$(Mn, Fe)$_x$Nb$_{3+x}$O$_{15}$ for x=0.00, 0.25, 0.50, 0.75 and 1.00. Samples were prepared by solid state reaction using the following reagents which were dried prior to use at the temperatures indicated and stored in a desiccator: BaCO$_3$ (Sigma-Aldrich, 99+%, 180 °C), La$_2$O$_3$ (Acros, 99.%, 900 °C), TiO$_2$ (99.8%, Sigma-Aldrich, 900 °C), Mn$_2$O$_3$ (Aldrich, 99%, 400 °C),

Fe$_2$O$_3$ (Aldrich, 99+%, 400 °C), Nb$_2$O$_5$ (Sigma-Aldrich, 99.9%, 900 °C). Reagents were weighed out in the required proportions to give 2–3 g totals, mixed manually into a paste with acetone using an agate mortar and pestle, dried, pelleted and fired in air in a muffle furnace on Pt foil. Samples were heated slowly to 800 °C and then in steps to 1100 °C with intermittent cooling, grinding and repelleting. It was found that the effect of Mn and Fe was to increase the reaction rate and to reduce the synthesis temperature compared to the undoped, x=0, analogue. For phase analysis and structure determination, in-house powder X-ray diffraction (XRD) used a Stoë STADI P diffractometer, Cu $K\alpha_1$ radiation and either a curved image plate detector for initial characterisation studies, or a small linear position sensitive detector for Rietveld refinement. The Stoë software package WinXpow was used for general data analysis. Rietveld refinements used the GSAS suite of programs [15].

Pellets for electrical property measurements were pressed uniaxially, fired at 1100 °C for 6 h and coated on opposite faces with Au paste which was decomposed and hardened by gradually increasing the temperature to 800 °C. Pellet densities were typically in the range 87–90% of the theoretical fully dense values. Pellets were loaded into a conductivity jig and attached to Pt electrodes. Measurements were carried out in air over a wide temperature range using two measurement systems: for the range 10–320 K, a cryocooler with an Agilent 4294A impedance analyser was used over the frequency range 40 Hz–13 MHz; for measurements from room temperature to ∼800 °C, the jig was placed in a tube furnace and measurements in air made over the frequency range 10 Hz–1 MHz using a Hewlett Packard 4192A Impedance Analyser. Data analysis, including fitting to equivalent circuits used the ZView software.

3. Results and discussion

3.1. Structural characterisation

Commencing with Ba$_2$LaTi$_2$Nb$_3$O$_{15}$, single phase solid solution series containing partial or complete replacement of Ti by either Mn and Nb or Fe and Nb were obtained. XRD analyses suggested

that all samples were single phase and adopt a similar tetragonal structure. Fig. 2 demonstrates the increase in cell volume (due to a significant increase in a) as the smaller Ti^{4+} cation is replaced by larger Mn^{3+}/Fe^{3+} and Nb^{5+} cations (6-coordinate ionic radii are 0.605, 0.645, 0.645 and 0.64 Å, respectively) [16]. The formation of these two new Ti-free TTB phases with $x=1$ may indicate the possible formation of a large number of new phases with general formula $A_2A'MB_4O_{15}$: A=Ba, Sr; A'=rare earth; M=Mn, Fe and perhaps Al, Ga; B=Nb, Ta.

Structural refinements for the two end-member compositions with $x=1$, i.e. $Ba_2LaFeNb_4O_{15}$ and $Ba_2LaMnNb_4O_{15}$ were carried out. In both cases, XRD data were collected at room temperature and Rietveld refinements carried out in the centrosymmetric space group $P4/mbm$. This choice of space group is supported by permittivity results (see later) which indicate very little variation in permittivity with temperature and therefore, the almost complete absence of ferroelectricity in these phases. A statistical distribution of La^{3+} and Ba^{2+} over the two A sites was used in refinements as these cations have very similar X-ray scattering

powers. However, previous work using neutron powder diffraction data (NPD) on $Ba_2LaTi_2Nb_3O_{15}$ [9] showed that La^{3+} preferentially occupies the smaller 12-coordinate A' site whilst the 15-coordinate A site is occupied by Ba^{2+} (12-coordinate ionic radii of La^{3+} and Ba^{2+} are 1.36 and 1.61 Å, respectively) [16]. A similar Ba–La distribution might be expected for $Ba_2LaFeNb_4O_{15}$ and $Ba_2LaMnNb_4O_{15}$ but XRD data are not sensitive to this and so a statistical cation distribution was used in these refinements. The fractional occupancies of all oxygen sites were fixed at unity and their thermal parameters constrained to be equal.

The $3d$ transition metal cations and Nb^{5+} are sufficiently different in atomic number that XRD data should be sensitive to the cation distribution over the two B sites. Nb^{5+}, Fe^{3+} and Mn^{3+} are similar in size, but differ in charge and electron configuration and so some degree of cation ordering might be expected. Starting models had a statistical distribution of Nb and the trivalent cation on both B sites but as this distribution was refined, the fit improved and a slight preference of the trivalent $3d$ cation for the 8-fold $B(1)$ site was observed for both Mn and Fe analogues. The higher symmetry $B(2)$ site is occupied almost exclusively by Nb. The lower symmetry of the 8-fold $B(1)$ site may enable it to better accommodate mixed cation occupancy. Final atomic coordinates are listed in Table 1 and selected bond lengths in Table 2. The refinement profiles are shown in Fig. 3.

The structures of both $Ba_2LaMnNb_4O_{15}$ and $Ba_2LaFeNb_4O_{15}$ are qualitatively similar to the paraelectric $P4/mbm$ phase of $Ba_2LaTi_2Nb_3O_{15}$ at 400 K [9]. The A and A' sites are 15- and 12-coordinate, respectively, with comparable bond lengths for both $x=0$ and $x=1$ phases. The higher symmetry B site on the $2c$ (site symmetry $m.mm$) position is located at the centre-of-mass of the oxide polyhedron with four equivalent bonds in the equatorial plane and two equal bond lengths to apical oxide ions. This cation
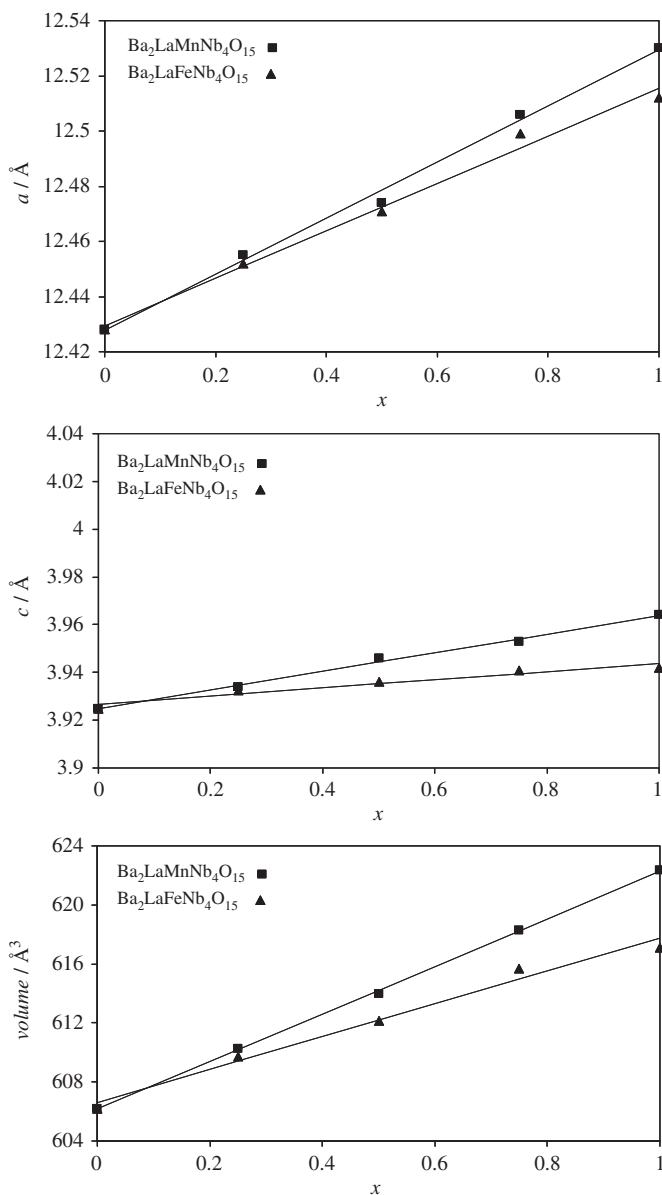

Fig. 2. Trends in lattice parameters a and c, and unit cell volume with x for $Ba_2LaTi_{2-2x}M_xNb_{3+x}O_{15}$; data for x=Mn shown as squares, for x=Fe as triangles.

Table 1

Final atomic parameters for $Ba_2LaMnNb_4O_{15}$ and $Ba_2LaFeNb_4O_{15}$ from Rietveld refinement using XRD data with space group $P4/mbm$, Ba/La(1) on $4g$ ($x,x+1/2,0$), Ba/La(2) on $2a$ (0,0,0), Nb/M(1) on $8j$ (x,y, 1/2), Nb/M(2) on $2c$ (0, 1/2,1/2), O(1) on $8j$ (x,y,1/2), O(2) on $4h$ ($x,x+1/2,1/2$), O(3) on $8j$ (x,y,1/2), O(4) on $8i$ (x,y,0) and O(5) on $2d$ (0,1/2,0).

		M=Mn	M=Fe
Ba/La(1)	x	0.1711(1)	0.17057(9)
	$U_{iso} \times 100$ (Å²)	2.86(8)	2.59(7)
	fractional occupancy	0.667/0.333	0.667/0.333
Ba/La(2)	$U_{iso} \times 100$ (Å²)	1.66(8)	1.10(6)
	fractional occupancy	0.667/0.333	0.667/0.333
Nb/M(1)	x	0.2142(1)	0.2149(1)
	y	0.9251(1)	0.9248(1)
	$U_{iso} \times 100$ (Å²)	0.81(7)	0.71(6)
	fractional occupancy	0.771(4)/0.229(4)	0.771(3)/0.229(3)
Nb/M(2)	$U_{iso} \times 100$ (Å²)	2.3(1)	2.5(1)
	fractional occupancy	0.91(1)/0.09(1)	0.92(1)/0.08(1)
O(1)	x	0.1601(1)	0.1588(9)
	y	0.5080(8)	0.5067(6)
O(2)	x	0.2843(9)	0.2841(7)
O(3)	x	0.370(1)	0.3653(7)
	y	0.565(1)	0.5639(9)
O(4)	x	0.2019(9)	0.2022(7)
	y	0.931(1)	0.9323(9)
O sites	$U_{iso} \times 100$ (Å²)	3.4(2)	2.3(1)
	a (Å)	12.5491(1)	12.5062(1)
	c (Å)	3.97008(5)	3.93826(6)
	R_{wp}	6.01%	4.54%
	R_p	5.43%	4.07%
	χ^2	0.90	1.089

Table 2
Selected bond lengths for $Ba_2LaMnNb_4O_{15}$ and $Ba_2LaFeNb_4O_{15}$ from Rietveld refinement using XRD data.

Bond	$M=$Mn	$M=$Fe
La/Ba(1)–O(1)	$4 \times 2.854(7)$	$4 \times 2.846(5)$
La/Ba(1)–O(2)	$2 \times 2.83(1)$	$2 \times 2.813(9)$
La/Ba(1)–O(3)	$4 \times 3.455(9)$	$4 \times 3.404(7)$
La/Ba(1)–O(4)	$2 \times 3.28(1)$	$2 \times 3.30(1)$
La/Ba(1)–O(4)	$2 \times 3.41(1)$	$2 \times 3.38(1)$
La/Ba(1)–O(5)	$1 \times 3.036(2)$	$1 \times 3.017(1)$
La/Ba(2)–O(3)	$8 \times 2.697(7)$	$8 \times 2.712(6)$
La/Ba(2)–O(4)	$4 \times 2.68(1)$	$4 \times 2.667(8)$
Nb/M(1)–O(1)	$1 \times 1.89(1)$	$1 \times 1.88(1)$
Nb/M(1)–O(2)	$1 \times 1.974(6)$	$1 \times 1.961(4)$
Nb/M(1)–O(3)	$1 \times 1.99(1)$	$1 \times 2.01(1)$
Nb/M(1)–O(3)	$1 \times 2.05(1)$	$1 \times 2.03(1)$
Nb/M(1)–O(4)	$2 \times 1.992(1)$	$2 \times 1.9776(8)$
Nb/M(2)–O(1)	$4 \times 2.01(1)$	$4 \times 1.99(1)$
Nb/M(2)–O(5)	$2 \times 1.98504(3)$	$2 \times 1.96913(3)$

site is slightly larger in the $x=1$ Mn and Fe analogues than in $Ba_2LaTi_2Nb_3O_{15}$, presumably as a result of substituting the smaller Ti^{4+} cation by slightly larger Nb^{5+} cation at this site. The lower symmetry B cation site on the $8j$ (site symmetry $m..$) position is again similar to that in $Ba_2LaTi_2Nb_3O_{15}$ at 400 K, with two equivalent bonds to apical oxide anions and four inequivalent bonds in the equatorial plane. The B cation appears to be displaced, on average, from the centre-of-gravity of the BO_6 polyhedron towards the empty trigonal channels (C sites); consequently, this $8j$ site may be better able to accommodate a mixture of cations with different bonding requirements. In addition, cation polarisation within this polyhedron may be responsible for the high permittivity (see later).

3.2. Electrical characterisation

A typical impedance data set for the Mn $x=1$ phase, $Ba_2LaMnNb_4O_{15}$, is shown in Fig. 4; the data are presented in

a $Ba_2LaMnNb_4O_{15}$
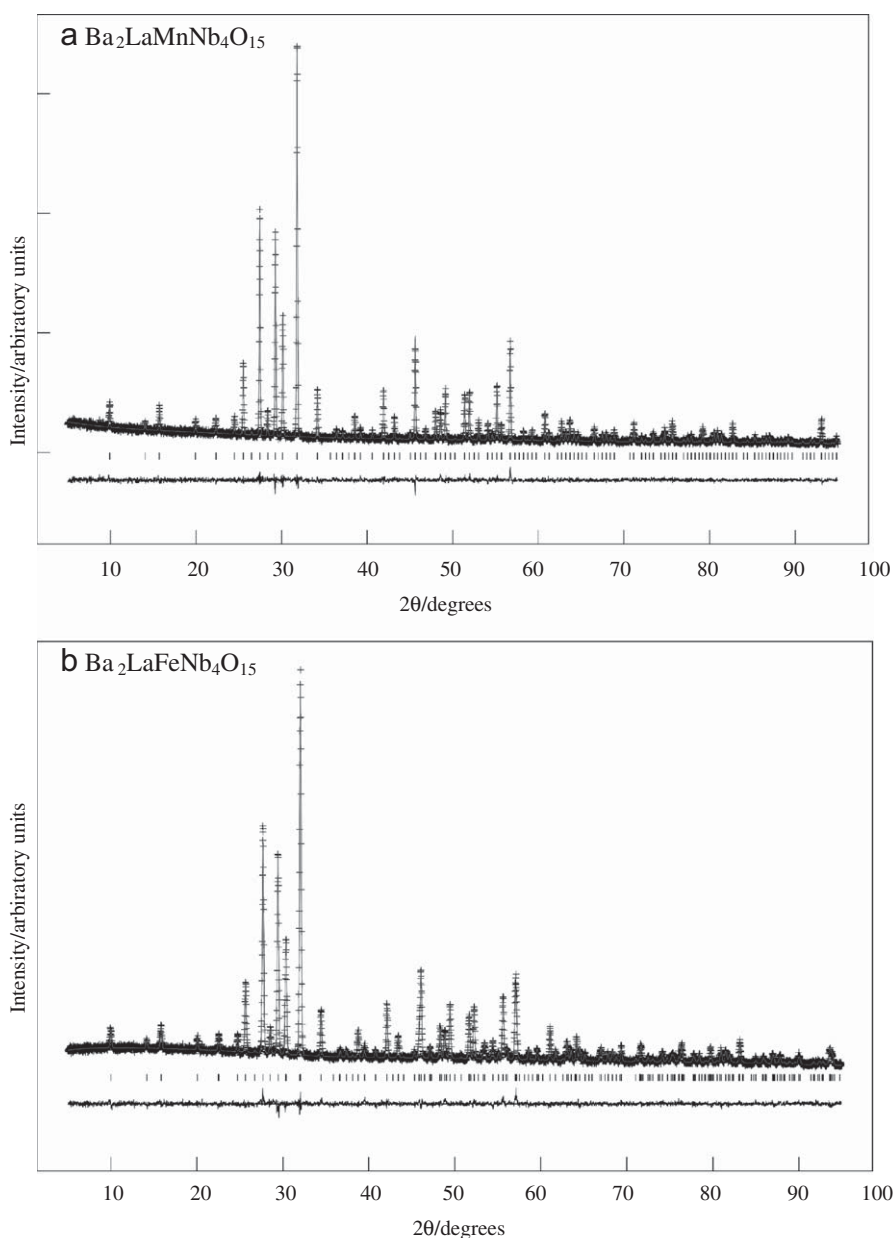

b $Ba_2LaFeNb_4O_{15}$

Fig. 3. Profiles from Rietveld refinement of (a) $Ba_2LaMnNb_4O_{15}$ and (b) $Ba_2LaFeNb_4O_{15}$ using room temperature XRD data; calculated $(-)$ and experimental $(+)$ patterns are shown above, ticks $(|)$ mark reflection positions and the difference line is shown below.
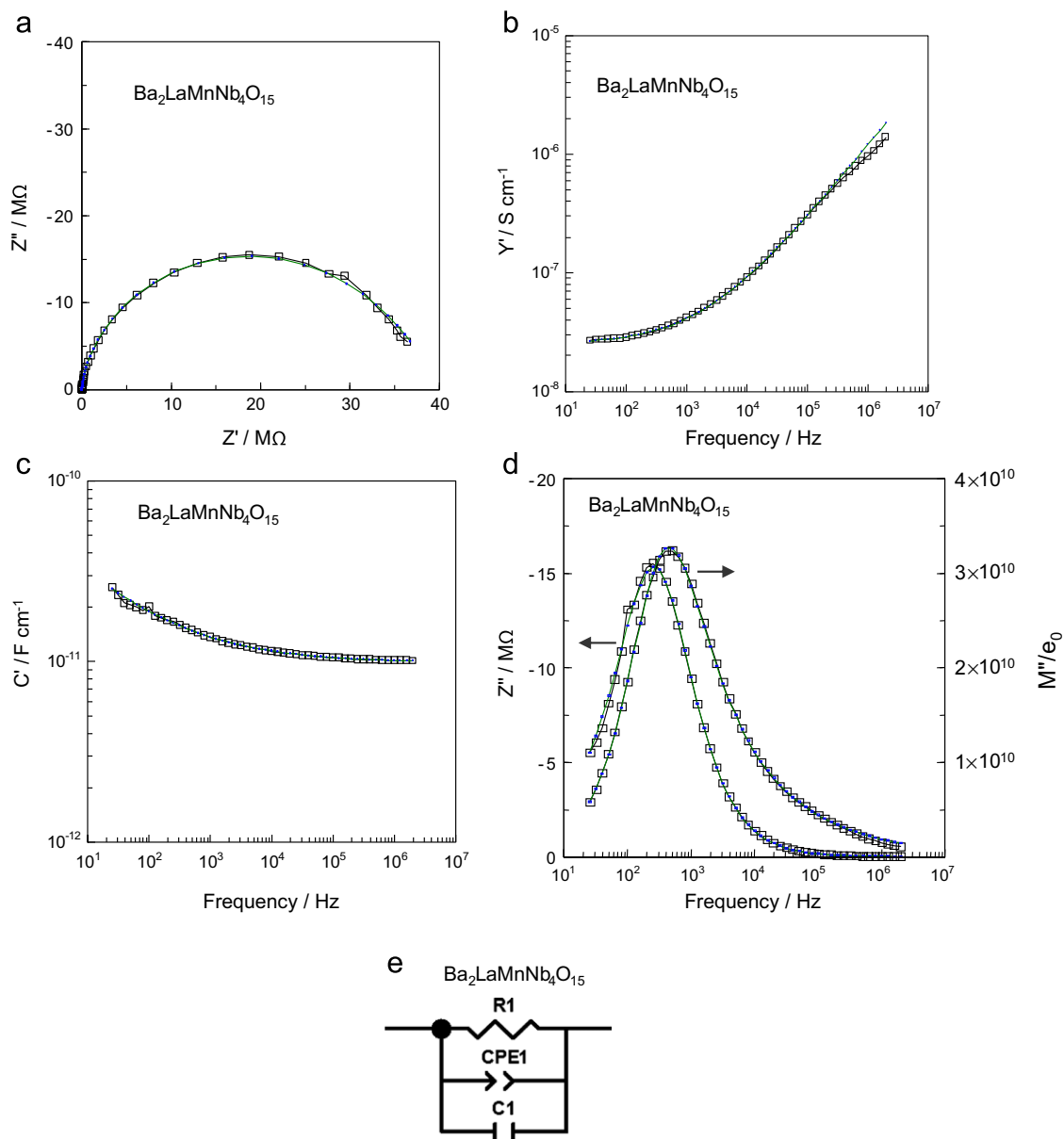
Fig. 4. Impedance spectroscopy data at 320 K for $Ba_2LaMnNb_4O_{15}$ showing experimental data points and results from fitting (—) to the equivalent circuit shown in (e) with resistance $R1$, capacitance $C1$ and constant phase element CPE1. (a) impedance complex plane plot; (b) Y', (c) C', (d) Z'' and M'' spectroscopic plots.

different formats in order to fully characterise the electrical microstructure of the sample and be able to extract values for the permittivity, ε' and dc conductivity, σ of the sample bulk. The impedance complex plane plot 4(a), shows a single, almost ideal semicircular arc with no evidence at higher or lower temperatures of additional arcs. A spectroscopic plot of the real part of the admittance, Y', shows a frequency independent plateau attributed to the dc conductivity, R^{-1}, at low frequencies, with frequency-dependent power law behaviour at higher frequencies, 4(b). The data shown indicate parts of both regions; at higher temperatures the dc plateau dominates the data, whereas at lower temperatures the power law response dominates. From the same data set, capacitance data, C', are shown as a function of frequency in Fig. 4(c); data show a frequency independent plateau at high frequency, attributed to the limiting high frequency capacitance of the sample C_1, with the onset of a small frequency dispersion at lower frequencies. Data are presented in the form of Z''/M'' spectroscopic plots in Fig. 4(d); a single, almost coincident peak is observed in both spectra, indicating that the sample can be

represented by a single electrical circuit element and therefore, is electrically homogeneous.

From consideration of these impedance data and their presentation in different formalisms, it was found that the equivalent circuit shown in Fig. 4(e) could be used to accurately fit the data, as shown in Figs. 4(a–d), over almost the entire temperature range 200–320 K; at temperatures below 200 K, the material was too resistive for arcs in Z^* to be measured and Y' data were noisy. Values for the permittivity ε' were obtained from $\varepsilon' = C'/C_0$, where C_0 is the vacuum capacitance of the conductivity jig. This analysis showed that the measured electrical properties correspond to the bulk response of the samples with little evidence for significant grain boundary impedances. The constant phase element, CPE1, in Fig. 4(e) contributes the high frequency power law dispersion to the Y' data, 4(b), and the low frequency dispersion to the C' data, 4(c). Inclusion of the CPE in the data fitting allows accurate values of R_1 and C_1 to be extracted from the data.

Permittivity data are shown in Fig. 5 for $Ba_2LaFeNb_4O_{15}$ and $Ba_2LaMnNb_4O_{15}$. These data were taken from the frequency

independent plateau values, as shown in Fig. 4(c). The data for the Fe phase pass through a very broad maximum at ∼40 K with a value of 105 and show a gradual decrease with increasing temperature, reaching a value of ∼80 at 320 K. Data for the Mn phase pass through a broad maximum with a value of ∼150 at ∼240 K and show a gradual decrease with decreasing temperature to a value of ∼100 at 10 K. These data may be compared with those for $Ba_2LaTi_2Nb_3O_{15}$, Fig. 6, which pass through a broad maximum at 200 K with a permittivity value of 300. $Ba_2LaTi_2Nb_3O_{15}$ is, however, a relaxor ferroelectric in which the permittivity values are frequency-dependent (not shown). Data are also shown in Fig. 6 for samples with 50% substitution of Ti by (Mn, Fe+Nb). For 50% Fe substitution, the permittivity maximum is greatly depressed and displaced to lower temperatures, peaking at ∼140 K. For 50% substitution of Mn, the permittivity is also greatly reduced and the maximum is displaced to slightly higher temperatures. The behaviour of these two compositions with 50% substitution, $x=0.5$, is therefore intermediate between those of the end members $x=0$ and $x=1$.

The partially and fully Mn, Fe-substituted phases retain significant polarisability in their structures since they have high ε' values but the cooperative displacements that are responsible for the permittivity maximum in $Ba_2LaTi_2Nb_3O_{15}$ are largely absent with 50% substitution of Ti and essentially completely absent for 100% substitution. In $Ba_2RETi_2Nb_3O_{15}$, it was presumed but not confirmed that both Nb and Ti, on both $B(1)$ and $B(2)$ sites are polar cations that contribute to the ferroelectric domains below T_C, especially in the phases containing small RE ions. For $RE=La$, relaxor behaviour is observed, rather than sharp, first order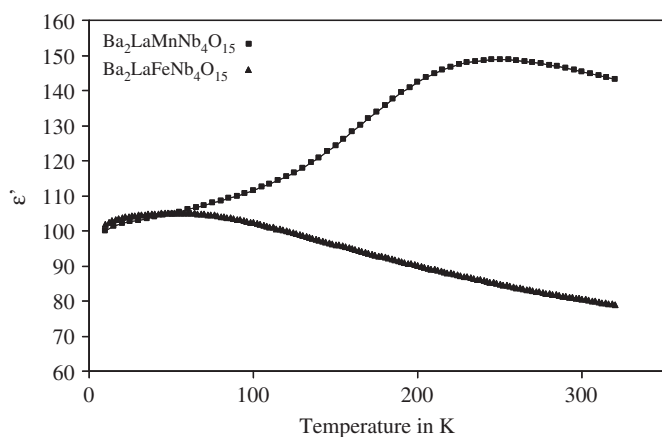 permittivity maxima. In this case, the domain structure is perturbed, presumably through loss of cooperative displacements of both Nb and Ti, or of both $B(1)$ and $B(2)$ sites simultaneously. In the two new Fe/Mn analogues reported here, the cooperative displacements are essentially destroyed. One interpretation is that the polar Ti^{4+} cations have been completely replaced and any polar fluctuations associated with (Fe, Mn) and Nb is insufficient to lead to cooperative displacements and polar domain formation.

Conductivity data for the new phases are shown in Arrhenius format in Fig. 7. $Ba_2LaFeNb_4O_{15}$ is highly resistive with a conductivity ∼1×10^{-6} ohm^{-1} cm^{-1} at 800 K. $Ba_2LaMnNb_4O_{15}$ is somewhat more conductive with a room temperature conductivity ∼1×10^{-8} ohm^{-1} cm^{-1}. The insulating nature of the samples indicates that there are no mobile carriers present, which is a strong indicator that Fe and Mn are present in a single oxidation state, 3+, consistent with the overall stoichiometry of the phases. For possible dielectric applications, an important practical parameter is the dielectric loss or $\tan\delta$ and values at 10^5 Hz are shown in Fig. 8 for both phases. The $\tan\delta$ for $Ba_2LaFeNb_4O_{15}$ is particularly small, <0.001 over the temperature range 120–320 K.

4. Conclusions

Two new phases, $Ba_2LaMNb_4O_{15}$: M=Mn, Fe have been synthesised and shown to have centrosymmetric tetragonal tungsten bronze crystal structures with space group $P4/mbm$. It is possible that a large number of related phases with this overall general formula may be synthesised. Both phases are high permittivity dielectrics; the dc conductivity of the Fe analogue and the ac conductivity represented as fixed frequency $\tan\delta$ data is extremely low, giving rise to possible microwave dielectric applications. These

Fig. 5. Permittivity as a function of temperature for $Ba_2LaMnNb_4O_{15}$ (data points shown as squares) and $Ba_2LaFeNb_4O_{15}$ (triangles) measured at 1×10^6 Hz.

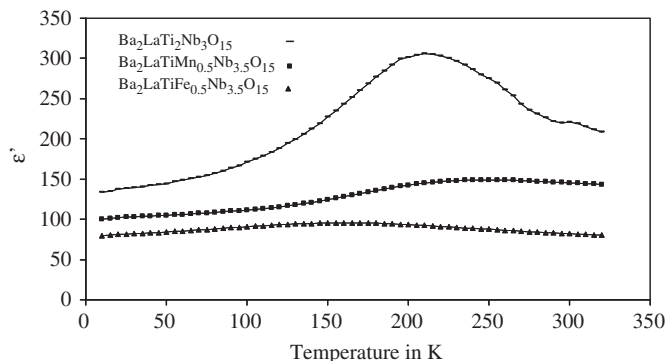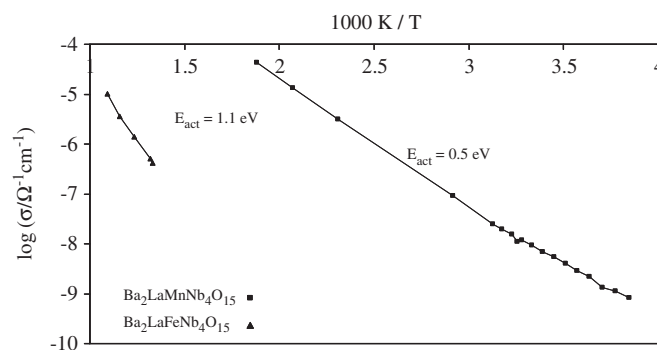**Fig. 6.** Permittivity as a function of temperature for $Ba_2LaTi_2Nb_3O_{15}$ (data points shown as dashes), $Ba_2LaTiMn_{0.5}Nb_{3.5}O_{15}$ (shown as squares) and $Ba_2LaTiFe_{0.5}Nb_{3.5}O_{15}$ (triangles) measured at 1×10^6 Hz.

Fig. 7. Arrhenius plots of $\log(\sigma)$ as a function of inverse temperature for $Ba_2LaMnNb_4O_{15}$ (■) and $Ba_2LaFeNb_4O_{15}$ (▲).
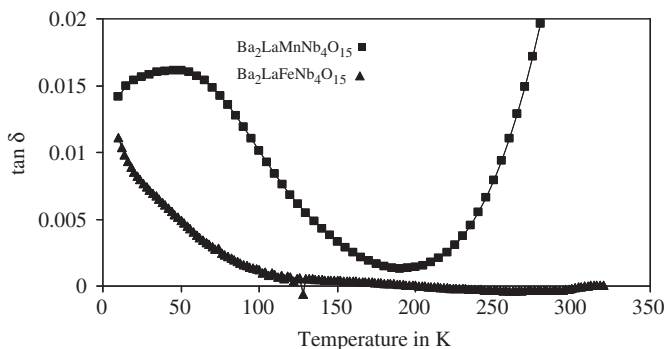
Fig. 8. Plot of $\tan\delta$ as a function of temperature $Ba_2LaMnNb_4O_{15}$ (■) and $Ba_2LaFeNb_4O_{15}$ (▲) measured at 1×10^5 Hz.

two new phases may be regarded, structurally, as derived from $Ba_2LaTi_2Nb_3O_{15}$ by a coupled substitution of (Mn, Fe+Nb) for Ti. The effect of this substitution is to dramatically reduce the relaxor ferroelectric properties of $Ba_2LaTi_2Nb_3O_{15}$, from which it may be proposed that Ti is the ferroelectrically-active cation and that even low concentrations of paramagnetic *B* site cations significantly diminish the ferroelectric behaviour of these materials.

Acknowledgment

Appendix A. Supplementary material

Supplementary data associated with this article can be found in the online version at doi:10.1016/j.jssc.2009.11.032.

References

[1] C.A. Randall, R. Guo, A.S. Bhalla, L.E. Cross, J. Mater. Res. 6 (8) (1991) 1720–1728.
[2] V. Bovtun, S. Kamba, S. Veljko, D. Nuzhnyy, K. Knizek, M. Savinov, J. Petzelt, J. Appl. Phys. 101 (2007) 054115.
[3] E. Garcia-Gonzales, A. Torres-Pardo, R. Jimenez, J.M. Gonzalez-Calbet, Chem. Mater. 19 (2007) 3575–3580.
[4] G.C. Miles, M.C. Stennett, D. Pickthall, C.A. Kirk, I.M. Reaney, A.R. West, Powder Diffr. 20 (1) (2005) 43–46.
[5] M.C. Stennett, G.C. Miles, J. Sharman, I.M. Reaney, A.R. West, J. Euro. Ceram. Soc. 25 (2005) 2471–2475.
[6] M.C. Stennett, I.M. Reaney, G.C. Miles, D.I. Woodward, A.R. West, C.A. Kirk, I. Levin, J. Appl. Phys. 101 (2007) 104114-1–104114-7.
[7] I. Levin, M.C. Stennett, G.C. Miles, D.I. Woodward, A.R. West, I.M. Reaney, Appl. Phys. Lett. 89 (2006) 122908.
[8] C.A. Kirk, M.C. Stennett, I.M. Reaney, A.R. West, J. Mater. Chem. 12 (2002) 2609–2611.
[9] G.C. Miles, M.C. Stennett, I.M. Reaney, A.R. West, J. Mater. Chem. 15 (2005) 798–802.
[10] N. Setter (Ed.), Piezoelectric materials in devices, EPFL Ceramics Laboratory, Lausanne, 2002.
[11] M. Prades, H. Beltran, N. Maso, E. Cordoncillo, A.R. West, J. Appl. Phys. 104 (10) (2008) 104118-1–104118-7.
[12] X.L. Zhu, X.M. Chen, X.Q. Liu, X.G. Li, J. Mater. Res. 23 (11) (2008) 3112–3121.
[13] E. Castel, M. Josse, F. Roulland, D. Michau, L. Raison, M. Maglione, J. Magn. Magn. Matter 321 (11) (2009) 1773–1777.
[14] A.J. Moulson, J.M. Herbert (Ed.), Electroceramics: Materials, Properties and Applications, Chapman and Hall, London, 1990.
[15] A.C. Larson, R.B.v. Dreele, GSAS, General Structure Analysis System, 2004.
[16] R.D. Shannon, Acta Cryst. A 32 (1976) 751–767.